

# What powers the radio emission in TDE AT2019dsg: a long-lived jet or the disruption itself?

Tatsuya Matsumoto,<sup>1,2,3\*†</sup> Tsvi Piran,<sup>1</sup> and Julian H. Krolik<sup>4</sup>

<sup>1</sup>*Racah Institute of Physics, Hebrew University, Jerusalem, 91904, Israel*

<sup>2</sup>*Research Center for the Early Universe, Graduate School of Science, University of Tokyo, Tokyo 113-0033, Japan*

<sup>3</sup>*Department of Physics, Graduate School of Science, University of Tokyo, Tokyo 113-0033, Japan*

<sup>4</sup>*Physics and Astronomy Department, Johns Hopkins University, Baltimore, MD 21218, USA*

10 May 2022

## ABSTRACT

The tidal disruption event, AT2019dsg, was observed across a broad range of electromagnetic-wavelengths from radio to X-rays, and it was possibly accompanied by a high-energy neutrino. We study the nature of the radio-emitting outflow by analyzing the synchrotron self-absorbed spectra in terms of the equipartition model. We find that the time evolution of the outflow radius can be interpreted as either free expansion or deceleration. If the former, the outflow was launched  $\simeq 40$  days before the optical peak; if the latter, the launch was  $\simeq 10$  days after the optical peak. In addition, the energy in the radio-emitting region increases over time. This second conclusion is most naturally interpreted by a scenario resembling the earliest stage of a supernova remnant: as more and more material is swept up, it is heated by the forward shock at the expense of the outflow’s kinetic energy. Energy injection from an accreting BH cannot be completely excluded, but the injection rate is very different from the fallback luminosity, requiring further physical explanation. If the neutrino association is real, the scale of energy injection needed is much greater than for the radio emission, suggesting that the detected neutrino did not arise from the radio emitting region.

**Key words:** transients: tidal disruption events

## 1 INTRODUCTION

A supermassive black hole (BH) lurking in a center of a galaxy can destroy a star approaching very close due to its strong gravity (Hills 1975; Rees 1988). Tidal disruption events (TDEs) have been observed in many wavelengths: X-rays (Saxton et al. 2020); UV/optical (Roth et al. 2020; van Velzen et al. 2020); and radio (Alexander et al. 2020). Understanding these observations will help us to take a census of the population of supermassive BHs, revealing their mass and spin distributions. It will also help us investigate relativistic effects around BHs by shedding light on the jet-launching mechanism, as well as stellar dynamics in galactic nuclear clusters (Stone et al. 2020).

However, the emission mechanisms of TDEs are still under debate. This is mainly because the evolution of bound debris, which finally accretes to the BH, is not well understood. For instance, although the observed luminosity in many TDEs is dominated by the UV/optical band, initial predictions estimated that it should be very weak (Rees 1988). Two models compete to explain it, one applicable if debris efficiently circularizes around the BH (Metzger & Stone 2016), the other if it does not (Piran et al. 2015). To resolve this issue, nu-

merical simulations and statistical studies using increasingly large samples (e.g. van Velzen et al. 2021) are in progress. In addition, a close examination of individual well-observed events is still useful for understanding TDEs.

AT2019dsg is one of the most well-observed TDEs. This event was discovered as a bright UV/optical TDE on 9 April 2019 by the Zwicky Transient Facility (van Velzen et al. 2021). Follow-up observation revealed rapidly declining X-rays  $\simeq 40$  days after the discovery (Cannizzaro et al. 2021; Stein et al. 2021) and radio emission lasting more than 500 days (Stein et al. 2021; Cendes et al. 2021; Mohan et al. 2021). In addition, IceCube reported detection of a high-energy neutrino in the same direction as the TDE (Stein et al. 2021), although the probability that this is actually associated with the TDE is not high. No TDE detected since ASASSN-14li (Miller et al. 2015; Alexander et al. 2016; Cenko et al. 2016; Holoien et al. 2016; Jiang et al. 2016; van Velzen et al. 2016; Brown et al. 2017) has such a rich set of multiwavelength data.

In this paper we focus on the radio, which is useful for studying the dynamics of outflow. The radio spectra have a peak, which is caused by the synchrotron self-absorption (SSA); applying the equipartition method to the time-dependence of the frequency of the peak and its luminosity, we can estimate both outflow properties and the density of the circumnuclear medium (CNM) surrounding the

\* E-mail: tatsuya.matsumoto@mail.huji.ac.il

† JSPS Research Fellow

BH (Chevalier 1998; Barniol Duran et al. 2013). Stein et al. (2021) and Cendes et al. (2021) carried out such an analysis and estimated the radius and energy in the radio-emitting site as well as the CNM density. Interestingly, they found that the energy in the emitting region increases with time. They attributed the increase to energy injection from the BH. We revisit this possibility and propose an alternative interpretation.

We organize this paper as follows. In §2 we review the equipartition method and estimate the physical quantities of the radio-emitting outflow. We analyze the time evolution of the equipartition radius in §3 and the CNM density profile in §4. In §5 we discuss the implications of the increasing energy of the radio-emitting region and find that, rather than indicating energy injection from the BH to the radio outflow, it is more naturally interpreted as the result of shock propagation in an impulsive event. We discuss the implications of our result for possible neutrino emission and the origin of the outflow in §6 and conclude this paper in §7.

## 2 THE EQUIPARTITION METHOD

We briefly review the equipartition method, which is applicable to a radio-emitting outflow with a spectral peak caused by the SSA (Pacholczyk 1970; Scott & Readhead 1977; Chevalier 1998; Barniol Duran et al. 2013). Consider an outflow producing synchrotron emission with an SSA spectral-peak flux density  $F_p$  at a frequency  $\nu_p$ . The equipartition method gives us the radius and energy of the radio-emitting region under the assumption that the post-shock thermal energy is distributed equally to relativistic electrons and magnetic field.

We follow the expressions for the radius and energy of Barniol Duran et al. (2013), but with corrections.<sup>1</sup> We assume that an arbitrary fraction of the dissipated kinetic energy is transferred to the electrons  $\epsilon_e$  and magnetic field  $\epsilon_B$  (see their equations 27 and 28 in the Newtonian limit):

$$R_{\text{eq}} \simeq 1 \times 10^{17} \text{ cm} \left[ 21.8 \times (525)^{p-1} \gamma_m^{2-p} \left( \frac{p+1}{3} \right) \right]^{\frac{1}{2p+13}} \left[ F_{p,\text{mJy}}^{\frac{p+6}{2p+13}} d_{L,28}^{\frac{2(p+6)}{2p+13}} \nu_{p,10}^{-1} (1+z)^{-\frac{3p+19}{2p+13}} \right] f_A^{-\frac{p+5}{2p+13}} f_V^{-\frac{1}{2p+13}} \left\{ (4\xi\epsilon) \frac{1}{2p+13} \right\}, \quad (1)$$

$$E_{\text{eq}} \simeq 1.3 \times 10^{48} \text{ erg} \left( \frac{2p+13}{17} \right) \left[ 21.8 \left( \frac{p+1}{3} \right) \right]^{-\frac{2(p+1)}{2p+13}} [(525)^{p-1} \gamma_m^{2-p}]^{\frac{11}{2p+13}} \left[ F_{p,\text{mJy}}^{\frac{3p+14}{2p+13}} d_{L,28}^{\frac{2(3p+14)}{2p+13}} \nu_{p,10}^{-1} (1+z)^{-\frac{5p+27}{2p+13}} \right] f_A^{-\frac{3(p+1)}{2p+13}} f_V^{\frac{2(p+1)}{2p+13}} \left\{ (4\xi) \frac{11}{2p+13} \left[ \frac{11}{2p+13} \epsilon^{-\frac{2(p+1)}{2p+13}} + \frac{2(p+1)}{2p+13} \epsilon^{\frac{11}{2p+13}} \right] \right\}. \quad (2)$$

Here the observables are the power-law index of the electron

<sup>1</sup> We take into account an additional dependence on radius  $R$  in the relativistic electrons' energy,  $\propto R^{2(1-p)}$ , which is ignored by Barniol Duran et al. (2013). This adds minor correction factors in their original expressions.

distribution  $p$  (given by the spectral slope) and the luminosity distance corresponding to the redshift  $z$ ,  $d_L$ , as well as  $F_{p,\text{mJy}} (= F_p/\text{mJy})$  and  $\nu_p$ . We use the notation  $Q_x = Q/10^x$  in cgs units unless otherwise specified.  $\gamma_m$  is the minimal Lorentz factor of relativistic electrons. In the standard prescription to estimate  $\gamma_m$  (e.g. Sari et al. 1998), it becomes less than unity for a non-relativistic outflow with a velocity  $v \lesssim v_{\text{DN}} \simeq 0.1 c [(p-2)\epsilon_{e,-1}/(p-1)]^{-1/2}$  (the so-called deep-Newtonian phase, Huang & Cheng 2003; Sironi & Ghisellini 2013).<sup>2</sup> In this phase, we set  $\gamma_m = 2$  because only relativistic electrons produce synchrotron emission. The area and volume-filling fractions of the outflow are defined so that the emission area and volume are given by  $f_A 4\pi R^2$  and  $f_V \pi R^3$ , respectively. We also define  $\epsilon \equiv [(\epsilon_B/\epsilon_e)/(2(p+1)/11)]$  and  $\xi \equiv 1 + \epsilon_e^{-1}$  (see below for the meanings of them).

The term ‘‘equipartition energy’’ is often used just for the sum of equally-distributed energy of the relativistic electrons and the accompanying magnetic field. However, the actual energy could be larger, and this possible increase is expressed by the terms in curly brackets in Eqs. (1) and (2) (besides a factor of 4 arising from a correction to the isotropic number of radiating electrons in the non-relativistic case). The factor  $\epsilon$  describes a deviation of the ratio of magnetic to electron energy from  $2(p+1)/11$ , the value for the minimal energy case. The factor  $\xi$  represents additional energy stored in the (hot) protons existing in the shocked region. With these corrections, the equipartition energy in Eq. (2) is the sum of the energy of (hot) protons, relativistic electrons, and magnetic field in the emitting site. Note that the outflow's total energy (including kinetic energy, for example) could be much larger, as we discuss later.

Importantly the factors  $\xi$  and  $\epsilon$  as well as the geometrical parameters  $f_A$  and  $f_V$  hardly influence  $R_{\text{eq}}$ , so this argument enables us to determine the emitting radius with only small uncertainty. The most significant dependence of  $R_{\text{eq}}$  comes from the covering fraction of the emitting region,  $f_A$ , and it is roughly given by  $R_{\text{eq}} \propto f_A^{-0.5}$ .

The Lorentz factor and number of radiating electrons at  $\nu_p$  are given by (equations 14 and 15 in Barniol Duran et al. 2013)

$$\gamma_e \simeq 525 F_{p,\text{mJy}} d_{L,28}^2 \nu_{p,10}^{-2} (1+z)^{-3} f_A^{-1} R_{\text{eq},17}^{-2}, \quad (3)$$

$$N_e \simeq 4.0 \times 10^{54} F_{p,\text{mJy}}^3 d_{L,28}^6 \nu_{p,10}^{-5} (1+z)^{-8} f_A^{-2} R_{\text{eq},17}^{-4}, \quad (4)$$

respectively. The (pre-shock) CNM density is estimated by dividing the total number of electrons by the volume swept up by the outflow:

$$n = \frac{N_e (\frac{\gamma_m}{\gamma_e})^{1-p} \max\left[\left(\frac{v_{\text{DN}}}{v}\right)^2, 1\right]}{\frac{\Omega}{3-k} R_{\text{eq}}^3} \simeq 4100 \text{ cm}^{-3} [525 \gamma_m^{-1}]^{p-1} F_{p,\text{mJy}}^{p+2} d_{L,28}^{2(p+2)} \nu_{p,10}^{-2p-3} \times (1+z)^{-3p-5} f_A^{-p-1} R_{\text{eq},17}^{-2p-5} \Omega^{-1} (3-k) \max\left[\left(\frac{v_{\text{DN}}}{v}\right)^2, 1\right]. \quad (5)$$

Here three correction factors arise. First, most relativistic electrons have Lorentz factor  $\sim \gamma_m$ , and their number is  $(\gamma_m/\gamma_e)^{1-p}$  times larger than  $N_e$ . Second, when the outflow is in the deep-Newtonian phase, only a fraction  $(v/v_{\text{DN}})^2$  of

<sup>2</sup> When the outflow expands at larger velocity than  $v \gtrsim v_{\text{DN}}$ ,  $\gamma_m$  depends on the outflow velocity and we have to determine  $R_{\text{eq}}$  and  $v$  at the same time.

**Table 1.** Radio data and results of our equipartition analysis for AT2019dsg. The time  $\Delta t$  is measured since the discovery in the observer frame (9 April 2019), which is different from that in Cendes et al. 2021 who set the origin as 10 days before the discovery. The equipartition radius, energy, Lorentz factor and total number of emitting electrons at  $\nu_p$ , and CNM density are calculated by Eqs. (1) - (5). We adopt two (freely-coasting and decelerating) velocity models given by fitting the time evolution of  $R_{\text{eq}}$ , and the corresponding density slope  $k$ . The spectra of the first two epochs are not of good quality and they are excluded from our analysis.

$\Delta t$ [d]	$F_p$ [mJy]	$\nu_p$ [10GHz]	$R_{\text{eq}}$ [ $10^{16}$ cm]	$E_{\text{eq}}$ [ $10^{48}$ erg]	$\gamma_e$	$N_e$ [ $10^{50}$ ]	$n$ (freely-coasting) [ $\text{cm}^{-3}$ ]	$n$ (decelerating) [ $\text{cm}^{-3}$ ]
(42)	$(0.47 \pm 0.06)$	$(1.29 \pm 0.30)$	$(1.04 \pm 0.25)$	$(1.19 \pm 0.50)$	$(59.05 \pm 4.71)$	$(0.83 \pm 0.26)$	$(22.29 \pm 20.02)$	$(12.68 \pm 11.39)$
(45)	$(0.56 \pm 0.06)$	$(1.62 \pm 0.49)$	$(0.90 \pm 0.27)$	$(1.17 \pm 0.53)$	$(59.62 \pm 4.76)$	$(0.80 \pm 0.29)$	$(34.01 \pm 38.37)$	$(22.04 \pm 24.87)$
50	$0.74 \pm 0.02$	$1.62 \pm 0.15$	$1.02 \pm 0.10$	$1.63 \pm 0.54$	$60.53 \pm 4.84$	$1.09 \pm 0.20$	$32.01 \pm 14.21$	$24.74 \pm 10.98$
70	$0.78 \pm 0.04$	$1.07 \pm 0.12$	$1.59 \pm 0.20$	$2.63 \pm 0.90$	$60.70 \pm 4.86$	$1.75 \pm 0.36$	$13.82 \pm 7.09$	$16.81 \pm 8.62$
72	$0.74 \pm 0.02$	$1.05 \pm 0.07$	$1.58 \pm 0.13$	$2.53 \pm 0.82$	$60.53 \pm 4.84$	$1.69 \pm 0.30$	$13.35 \pm 5.15$	$16.78 \pm 6.47$
120	$1.30 \pm 0.06$	$0.89 \pm 0.08$	$2.43 \pm 0.25$	$5.85 \pm 1.96$	$62.41 \pm 5.04$	$3.71 \pm 0.71$	$8.55 \pm 3.84$	$18.31 \pm 8.22$
151	$1.11 \pm 0.03$	$0.79 \pm 0.07$	$2.53 \pm 0.26$	$5.43 \pm 1.80$	$61.88 \pm 4.98$	$3.49 \pm 0.66$	$7.03 \pm 3.13$	$18.59 \pm 8.28$
178	$1.38 \pm 0.04$	$0.50 \pm 0.05$	$4.44 \pm 0.45$	$11.17 \pm 3.71$	$62.61 \pm 5.05$	$7.05 \pm 1.33$	$2.67 \pm 1.19$	$8.16 \pm 3.64$
290	$0.89 \pm 0.04$	$0.38 \pm 0.04$	$4.76 \pm 0.59$	$8.70 \pm 2.95$	$61.14 \pm 4.91$	$5.72 \pm 1.16$	$1.69 \pm 0.87$	$7.78 \pm 3.98$
551	$0.38 \pm 0.04$	$0.18 \pm 0.05$	$6.80 \pm 1.78$	$6.69 \pm 2.80$	$58.38 \pm 4.64$	$4.76 \pm 1.53$	$0.44 \pm 0.43$	$3.40 \pm 3.30$

electrons are accelerated to relativistic energy (Sironi & Giannios 2013; Matsumoto & Piran 2021a). Third, the density is assumed to follow  $n \propto R^{-k}$  ( $k < 3$ ), and the total electron number in the volume swept-up by the outflow with a constant solid angle  $\Omega$  is given by  $\int_0^R \Omega r^2 n(r) dr = \Omega n(R) R^3 / (3 - k)$ . The index  $k$  is known only after the density profile is calculated without this factor. When the density profile is not described by a power-law function, we can approximate the integral as  $\simeq \Omega n(R) R^3$ , which is justified as long as  $d \log n / d \log r < 3$ .

We apply the equipartition method to AT2019dsg using the peak fluxes and frequencies in Table 1 taken from Stein et al. (2021) and Cendes et al. (2021). The other observables are  $z = 0.051$ , the corresponding luminosity distance  $d_L \simeq 230$  Mpc, and the power-law index  $p = 2.7 \pm 0.2$ . We adopt the same parameters as those of Cendes et al. (2021), who assumed that the outflow is spherical ( $\Omega = 4\pi$ ), and the emitting region is a shell with the width of  $dR = 0.1 R_{\text{eq}}$ . These assumptions give  $f_A = 1$  and  $f_V = 0.36$ . The other parameters are  $\epsilon_e = 0.1$ ,  $\epsilon_B = 0.02$ , and  $\gamma_m = 2$  (assuming  $v < v_{\text{DN}}$ , which is justified later). The results are shown in Table 1, which are basically consistent with those of Cendes et al. (2021) except for the CNM density; in that estimate, they neglected the correction factor  $(v/v_{\text{DN}})^2$ . For the outflow velocity, we use two (freely-coasting and decelerating) models motivated by fitting the time evolution of  $R_{\text{eq}}$  (see the next section). We also adopt the density slope  $k$  obtained by fitting the calculated profile.

### 3 LAUNCH TIME OF THE RADIO-OUTFLOW

Fitting the time evolution of the equipartition radius, we derive the velocity and launching time of the radio-emitting outflow (hereafter radio-outflow). Fig. 1 depicts the equipartition radius at each observation time. Since the quality of the data at 42 and 45 days after the discovery is too poor to determine the spectral peak, we do not include these observations in the following calculation. The frequency of the peak is also somewhat difficult to determine in the  $\Delta t = 551$  d data, but we include it in analysis with a sizable error bar.

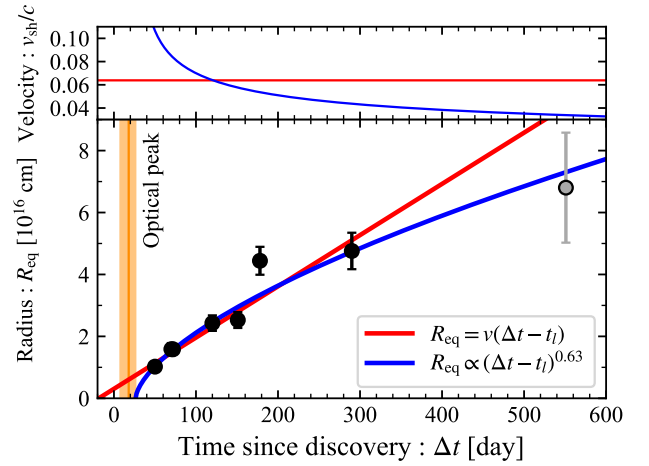


**Figure 1.** (Bottom) Equipartition radius at each observation epoch. The red and blue curves denote the best-fit curves of freely-coasting and decelerating models, respectively, with key parameters of  $v_{\text{sh}} \simeq 0.064 c$  and  $t_l \simeq -18$  d (freely-coasting) and  $\alpha = 0.63$  and  $t_l = 26$  d (decelerating). The quality of spectrum at 551 days is not so good and we use a gray dot to highlight this. The orange shaded region shows the peak time of optical emission. (Top) Outflow velocity derived by time derivative of the best-fit models of  $R_{\text{eq}}$ .

We consider two evolution models. The first is a freely-coasting outflow:  $R_{\text{eq}} = v_{\text{sh}}(\Delta t - t_l)$ , where  $\Delta t$  and  $t_l$  are the observation time and outflow-launching time, respectively, and both of them are measured since the discovery. The best-fit parameters are  $v_{\text{sh}} = 0.064_{-0.005}^{+0.005} c \simeq 20000_{-1500}^{+1500} \text{ km s}^{-1}$  and  $t_l = -18_{-11}^{+9}$  d (the error represents  $1\sigma$ ), giving a reduced chi-square of  $\chi_r^2 \simeq 2.2$ . The second is a decelerating (or accelerating) outflow with  $R_{\text{eq}} = A(\Delta t - t_l)^\alpha$ . The best-fit parameters are  $t_l = 26_{-18}^{+11}$  d and  $\alpha = 0.63_{-0.12}^{+0.16}$  with a reduced  $\chi_r^2 \simeq 1.8$ ; hence, deceleration is favored, as found by Cendes et al. (2021). However, the distinction in  $\chi_r^2$  depends entirely on the  $\Delta t = 551$  d observation, which has a large uncertainty.

It should be noted that for both models the best-fit launching time  $t_l$  is independent of the equipartition parameters  $\epsilon$ ,  $\xi$ ,  $f_A$ , and  $f_V$  (Krolik et al. 2016) while the other parameters  $v_{\text{sh}}$  and  $A$  depend on them. These best-fit curves are shown in Fig. 1.

The top panel of Fig. 1 depicts the velocity of each model as a function of time, deriving it from  $v_{\text{sh}} \equiv dR_{\text{eq}}/d(\Delta t)$ . Strictly speaking, this quantity represents not the outflow velocity but the shock velocity. The actual outflow velocity is a little smaller than the shock velocity; their ratio is given by the shock jump condition (e.g. Landau & Lifshitz 1987):  $\zeta \equiv v_{\text{sh}}/v = (\hat{\gamma} + 1)/2$ , where  $\hat{\gamma}$  is the adiabatic index of the shocked material. For  $\hat{\gamma} = 5/3$ , this factor is order unity,  $\zeta = 4/3$ , but this correction is important for inferring the origin of the outflow.

The outflow-launching time  $t_l$  can also constrain the origin of the radio outflow. We define it using the peak time of the optical emission as a reference time and taking the time difference between the outflow’s launch and the optical peak. The optical luminosity peaked at around 27 April 2019, or  $18_{-10}^{+8}$  days after discovery (van Velzen et al. 2021). For the freely-coasting model, the optical peak was  $36_{-10}^{+8}$  days after the outflow-launch. On the other hand, for the decelerating model the optical peak precedes the outflow-launch by  $8_{-8}^{+10}$  days (Here we used the central values of  $t_l$ . If we add errors of  $t_l$  assuming a Gaussian distribution with  $\sigma \simeq 10$  and 15 d the launching time has an error of  $\simeq 13$  and 17 d for each model). We will discuss the implication of these time differences for the origin of the radio outflow in §6.

#### 4 THE CNM DENSITY PROFILE

Radio observations of TDEs provide possibly the only way to infer the CNM density distribution around distant galaxies (e.g. Alexander et al. 2016; Krolik et al. 2016). Fig. 2 depicts the profiles reconstructed by our equipartition analysis. The two thick colored curves represent the predictions made by our two outflow models (note that the estimate of the CNM density depends on the outflow velocity, see Eq. 5). The velocities are derived from the best-fit models of the equipartition radius,  $v = \zeta^{-1} dR_{\text{eq}}/d(\Delta t)$ . Fitting the density profiles with a power-law function, we find the best fits for  $n \propto R^{-1.99}$  and  $R^{-0.83}$  for the freely-coasting and decelerating models, respectively. Our density values are slightly larger than those of Cendes et al. (2021), mainly because we consider the deep-Newtonian correction,  $(v/v_{\text{DN}})^2$ .

The CNM profiles of our Galactic center and the host galaxies of two other radio TDEs, ASASSN-14li (Alexander et al. 2016; Krolik et al. 2016) and CNSS J0019+00 (Anderson et al. 2020) are shown in Fig. 2. The latter two are derived by the same procedure that we used for AT2019dsg. Their equipartition radii evolve at a constant velocity of  $v_{\text{sh}} \simeq 0.03c$ . The CNM densities in all the TDE host galaxies are larger than in Sgr A\*. The CNM density profile of AT2019dsg is shallower than in the other TDEs; this contrast is related to the different time evolution of its equipartition energy.

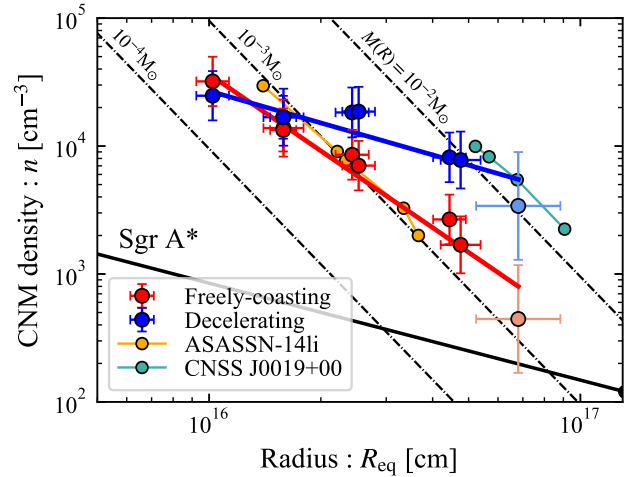


**Figure 2.** CNM density profiles reconstructed from the equipartition analysis. Red and blue line shows the best-fit power-law functions for the freely-coasting ( $n \propto R^{-1.99}$ ) and decelerating ( $n \propto R^{-0.83}$ ) models for AT2019dsg, respectively. Profiles of Milky Way ( $n \propto R^{-1}$ , Baganoff et al. 2003; Gillessen et al. 2019) and other TDEs ( $n \propto R^{-2.5}$ ) are also presented. Black dash-dotted lines show the positions where the enclosed mass of  $M(R) \simeq 4\pi m_p n R^3 = 10^{-4} - 10^{-2} M_{\odot}$ .

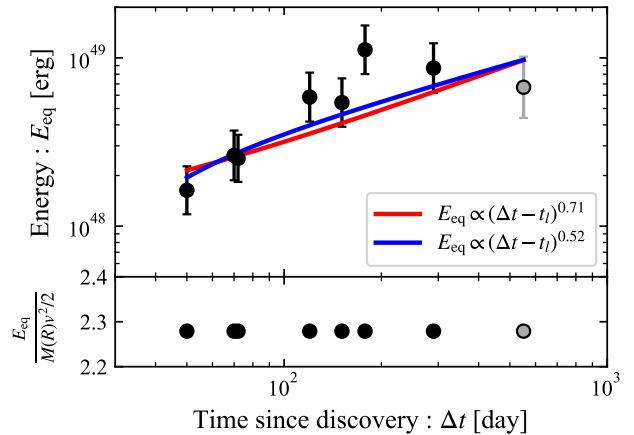


**Figure 3. (Top)** Equipartition energy at each observation epoch. The red and blue curves represent the best-fit power-law functions with the same outflow-launching time as the freely-coasting ( $t_l = -18$  d) and decelerating (26 d) outflow models, respectively. **(Bottom)** Ratio of equipartition energy to the kinetic energy.

#### 5 ENERGY INJECTION FROM THE BH?

We now address the question raised in the Introduction: Is energy continually injected into the outflow, as inferred by Stein et al. (2021) and Cendes et al. (2021)? To answer this question, we fit the time evolution of  $E_{\text{eq}}$  by a power-law function  $E_{\text{eq}} \propto (\Delta t - t_l)^{\beta}$  using the same  $t_l$  obtained from the fits to  $R_{\text{eq}}$ . The best-fit power-law indices are  $\beta = 0.71_{-0.15}^{+0.14}$  and  $0.52_{-0.11}^{+0.10}$  for the freely-coasting and deceleration models, respectively (see top panel in Fig. 3). Stein et al. (2021) and



Cendes et al. (2021) found that the equipartition energy increases as  $E_{\text{eq}} \propto \dot{t}$  and  $\dot{t}^{1.5}$ , respectively, where  $\dot{t}$  is the time measured since their own origins. They found faster energy increase because they used data points only up to 178 days, but we agree that the energy within the radio-producing region increases as time goes on.

Stein et al. (2021) and Cendes et al. (2021) suggested that the increase is caused by a continuous energy injection to the shocked region from the accreting BH. In the following paragraphs, we show that that the observations do not necessarily imply this. In fact, although we cannot rule it out, we demonstrate that this interpretation is unlikely. Consider, first, the freely-coasting (constant velocity) model. Like a supernova remnant, the first stage of the interaction between the outflow and the surrounding matter involves a combination of two shocks: a forward shock propagating into the CNM and a reverse shock propagating into the outflow. Their post-shock regions are separated by a contact discontinuity. As long as the mass of the outflow is significantly larger than the shocked CNM mass, the system effectively does not slow down. As more CNM is swept up and heated by the forward shock, more energy is transferred to the shocked region at the expense of the very large kinetic energy of the outflow.<sup>3</sup> This energy transfer appears as an increase of the energy of the relativistic electrons and magnetic field, and hence as an increase of the equipartition energy. This phase of outflow-CNM interaction most naturally explains the observation of AT2019dsg.

More precisely, the velocity of the shocked region is determined by energy conservation:

$$E_{\text{kin}}(> v) = [M_{\text{ej}}(> v) + M(R_{\text{eq}})]v^2/2, \quad (6)$$

where we suppose that the outflow is ejected with a spread of velocities, with kinetic energy and mass distributions  $E_{\text{kin}}(> v)$  and  $M_{\text{ej}}(> v)$ . The CNM mass swept-up by an isotropic outflow is approximated by

$$M(R) \simeq 4\pi m_p n R^3. \quad (7)$$

In the freely-coasting phase, as long as the outflow mass dominates the total mass,  $M_{\text{ej}}(> v) \gg M(R_{\text{eq}}) \simeq 3 \times 10^{-3} M_{\odot}$ , the velocity is almost constant. Therefore, the velocity structure should be very steep in this case (for instance,  $E_{\text{kin}}(> v) \propto v^{-l}$  with  $l \gg 1$ ) and the outflow may be characterized by a single velocity. On the other hand, the equipartition energy is given by

$$E_{\text{eq}} \sim m_p n f_V \pi R_{\text{eq}}^3 v^2 / 2 \propto M(R_{\text{eq}}) v^2. \quad (8)$$

Therefore, without any external energy injection, the equipartition energy naturally increases as more and more CNM is swept up and accumulates in the shocked region. To realize an energy increase with  $\beta = 0.71^{+0.14}_{-0.15}$  in the freely-coasting model, the density profile should have  $k = 2.29^{+0.15}_{-0.14}$ ,<sup>4</sup> that is consistent with our result,  $k = 1.99^{+0.28}_{-0.26}$ . It should be noted

<sup>3</sup> Energy loss by electron synchrotron cooling is negligible because the cooling timescale is much longer than the dynamical time,  $t_{\text{cool}} \simeq 4500 \text{ d} (B/G)^{-2} (\gamma_m/2)^{-1}$ , where the magnetic field is estimated by the equipartition analysis,  $B \simeq 0.1 - 1 \text{ G}$  (see also Cendes et al. 2021).

<sup>4</sup> For a given evolution of  $R_{\text{eq}} \propto t^\alpha$  and  $E_{\text{eq}} \propto t^\beta$ , we find these exponents are related to the slope of density profile by  $k = (5\alpha - \beta - 2)/\alpha$ .

that in Eq. (8), we assumed that the total energy in the emission region is proportional to the dissipated kinetic energy of the outflow. The bottom panel of Fig. 3 shows that the ratio of  $E_{\text{eq}}/[M(R_{\text{eq}})v^2/2]$  supports this assumption.

Although there is no motivation to consider external energy injection in the freely-coasting model, we can still consider such a scenario. In particular, suppose the BH launches a relativistic jet that increases the kinetic energy of the outflow as  $E_{\text{kin}} \propto t^m$  (here we define  $t \equiv \Delta t - t_l$ ). Depending on whether the outflow mass or swept-up CNM mass dominates the total mass, we obtain the time evolution of  $R_{\text{eq}}$ :

$$R_{\text{eq}} \propto \begin{cases} t^{\frac{m+2}{2}} & : M_{\text{ej}} > M(R_{\text{eq}}), \\ t^{\frac{m+2}{5-k}} & : M_{\text{ej}} < M(R_{\text{eq}}), \end{cases} \quad (9)$$

where we consider a power-law CNM distribution  $n \propto R^{-k}$  and approximate  $R_{\text{eq}} \sim v_{\text{sh}} t$ . In our fit with  $\alpha = 1$ , the former case corresponds to a ‘‘genuine’’ freely-coasting outflow,  $m = 2(\alpha - 1) = 0$ , which we have proposed above. The outflow mass must be larger than  $\gtrsim 3 \times 10^{-3} M_{\odot}$ . The latter case represents an injection scenario, where the outflow would have decelerated without the energy supply. We find here that  $m = \alpha(5 - k) - 2 = 1.01^{+0.26}_{-0.28}$ , similar to the value of  $\beta = 0.71^{+0.14}_{-0.15}$ . In this case, the outflow mass is constrained to be  $\lesssim 3 \times 10^{-4} M_{\odot}$ . However, as we have pointed out, there is no a priori reason why the engine should inject energy at this rate in order to keep the outflow velocity constant. These results are summarized in Table 2.

In the decelerating model, the swept-up CNM mass must be larger than the outflow mass,  $M(R) \gtrsim M_{\text{ej}}$ . Eq. (8) implies  $E_{\text{kin}} \propto E_{\text{eq}}$  and hence the energy in the shocked region increases. Again there are two possibilities for this increase. One is that it can arise from the kinetic energy of the outflow. Slower materials catch up with and inject energy to the shocked region (this scenario is similar to the scenario for the freely-coasting model). The CNM mass is comparable to the outflow mass  $M_{\text{ej}}(> v)$  in this case. Assuming the kinetic energy distribution  $E_{\text{kin}}(> v) \propto v^{-l}$  we obtain the evolution of the radius as  $R \propto t^{\frac{l+2}{5-k+l}}$ . The slope of the energy distribution is given by  $l = (2 + k\alpha - 5\alpha)/(\alpha - 1) \simeq 1.7$  and the energy distribution is inferred to be  $E_{\text{kin}}(> v) \simeq 10^{48} \text{ erg} (v/0.08c)^{-1.7}$  or equivalently  $M_{\text{ej}}(> v) \simeq 3 \times 10^{-4} M_{\odot} (v/0.08c)^{-3.7}$ . At the last epoch of observation, about  $\simeq 9 \times 10^{48} \text{ erg}$  has been injected in total. Again this scenario does not require any energy injection from the BH engine.

Another is continuous energy injection from the BH. In this case,  $M_{\text{ej}} \ll M(R)$  and the time evolution of the radius is given by Eq. (9). We find that the injected energy evolves as  $E_{\text{kin}} \simeq 10^{48} \text{ erg} (t/24 \text{ d})^{0.6}$  and the injection luminosity is given by  $\simeq 2 \times 10^{41} \text{ erg s}^{-1} (t/24 \text{ d})^{-0.4}$ , where the normalization corresponds to the first observation  $\Delta t = 50 \text{ d}$ . This luminosity is much smaller and decays rather slower than the fallback luminosity to the BH,  $\dot{M}_{\text{fb}} c^2 \sim 10^{47} \text{ erg s}^{-1} (t/24 \text{ d})^{-5/3} R_{*,0} M_{*,0}^{1/3} M_{\text{BH},6}^{-2/3}$  (Rees 1988; Phinney 1989), where  $R_*$ ,  $M_*$ , and  $M_{\text{BH}}$  are the disrupted stellar radius and mass, and the BH mass, respectively, normalized to solar values. We cannot exclude this possibility, but we do not see a simple physical explanation for this injection. Most importantly, it is much smaller than the injection rate inferred from the neutrino association (Stein et al. 2021; Winter & Lunardini 2021, see below).

**Table 2.** Possible types of energy injection for freely-coasting and decelerating radio-outflow models of AT2019dsg. The indices  $\alpha$ ,  $\beta$ , and  $k$  are obtained by fitting radius ( $R_{\text{eq}} \propto t^\alpha$ ), energy ( $E_{\text{eq}} \propto t^\beta$ ), and density profile ( $n \propto R^{-k}$ ), respectively. For each injection type, the inferred injection profiles are shown. These indexes are given by  $m = 2(\alpha - 1)$  for  $M_{\text{ej}} > M(R)$ ,  $m = \alpha(5 - k) - 2$  for  $M_{\text{ej}} < M(R)$ , and  $l = (2 + k\alpha - 5\alpha)/(\alpha - 1)$  (see text).

Model	Index			Type of energy injection		
	$\alpha$	$\beta$	$k$	$E_{\text{kin}} \propto t^m$ ( $M_{\text{ej}} > M(R)$ )	$E_{\text{kin}} \propto t^m$ ( $M_{\text{ej}} < M(R)$ )	$E_{\text{kin}} \propto v^{-l}$
Freely-coasting	1	$0.71^{+0.14}_{-0.15}$	$1.99^{+0.28}_{-0.26}$	$m = 0$ (Natural)	$m \simeq 1.0$ (Fine-tuning)	—
Decelerating	$0.63^{+0.16}_{-0.12}$	$0.52^{+0.10}_{-0.11}$	$0.83^{+0.28}_{-0.26}$	—	$m \simeq 0.6$ (Possible)	$l \simeq 1.7$ (Possible)

## 6 DISCUSSION

AT2019dsg coincides in position with the high-energy ( $\simeq 0.2$  PeV) neutrino IceCube-101001A detected on 1 October 2019 (175 days after the discovery, Stein et al. 2021). Stein et al. (2021) suggested that the neutrino was produced by a proton accelerated by a radio-emitting outflow whose energy is as large as  $\sim 10^{53}$  erg. This is much larger than the energy estimates based on the radio observations. This situation does not change even if we consider a conical outflow like a jet. Winter & Lunardini (2021) proposed that the neutrino was produced by an on-axis jet which continuously injects energy to the radio-emitting site. Similarly, their jet luminosity of  $\simeq 3 \times 10^{44}$  erg s $^{-1}$  and injected energy of  $\simeq 5 \times 10^{51}$  erg are three orders of magnitude larger than those implied by our estimates of the energy in the emitting region. The large discrepancy in energy could be resolved with very small equipartition parameters  $\varepsilon_e$  and  $\varepsilon_B$  are  $\lesssim 10^{-4}$ . However, the radio outflow would have been accelerated to relativistic velocity with these injection rates, which are inconsistent with the inferred emission radii from our equipartition analysis. Moreover, such a relativistic outflow was not seen by the VLBI observation (Mohan et al. 2021). Other scenarios where the neutrino production site is not related to the radio-emitting outflow (Hayasaki & Yamazaki 2019; Liu et al. 2020; Murase et al. 2020) are not constrained by our results.

Turning now to the origin of the radio outflow, there are two main channels to launch Newtonian outflows from TDEs. One is the unbound debris ejected at the moment of the disruption. The other is a disk wind launched when debris fallback forms an accretion disk. Because these outflows are launched at different times, it may be possible to discriminate between them on the basis of our inferred launching times,  $\simeq 40$  d before and  $\simeq 10$  d after the optical peak, for the freely-coasting and decelerating models, respectively. The distribution of the reduced chi-square is shown in Figs. 4 and 5 for each model.

These launch times can constrain the outflow’s origin when placed in the context of an optical emission model. According to the apocenter-shock model (e.g. Piran et al. 2015), the returning stream passes the pericenter having suffered little dissipation and collides with later-arriving material near the orbital apocenter. The optical emission arises from the apocenter shock, and it peaks when the most bound debris returns to the apocenter after its fallback time:<sup>5</sup>

$$t_{\text{fb}} \simeq 41 \text{ d } R_{*,0}^{3/2} M_{*,0}^{-1} M_{\text{BH},6}^{1/2}. \quad (10)$$

<sup>5</sup> Radiation diffusion from the shocked region can lengthen the timescale.

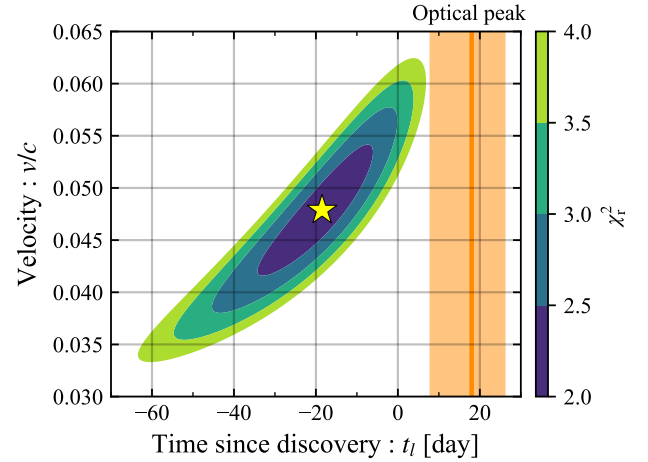


**Figure 4.** Distribution of the reduced chi-square for the freely-coasting model of  $R_{\text{eq}} = v(t - t_l)$ . The yellow star denotes the best-fit parameter set of  $v = v_{\text{sh}}/\zeta \simeq 0.05 c \simeq 15000$  km s $^{-1}$  and  $t_l \simeq -18$  d.

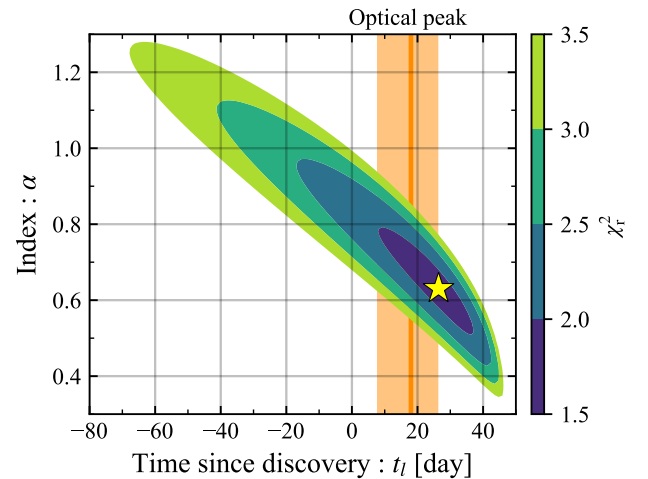


**Figure 5.** The same as Fig. 4 but for the deceleration model of  $R_{\text{eq}} \propto (t - t_l)^\alpha$ . The best-fit parameters are  $\alpha \simeq 0.63$  and  $t_l \simeq 26$  d.

Thus, the unbound debris is launched  $\sim t_{\text{fb}}$  before the optical peak. Ryu et al. (2020a) estimated the timescale  $t_{\text{fb}} = 29_{-4}^{+5}$  d within the apocenter-shock model,<sup>6</sup> which is consistent with our result  $\simeq 40$  d (freely-coasting model). However, the expected solid angle of the unbound debris is  $\Omega \sim 0.1 - 1$  (Krolik et al. 2016; Yalinewich et al. 2019), for which the implied velocity is  $\gtrsim 3$  times larger than the  $v \simeq 15000 \text{ km s}^{-1}$  estimated for  $\Omega = 4\pi$  (see Eq. 1 and the dependence on  $f_A \propto \Omega$ ). Such a velocity is too high for the unbound debris even if we consider a fast tail in the velocity distribution (Ryu et al. 2020b; Matsumoto & Piran 2021a). Note that the launching time is independent of the equipartition parameters.

The other optical emission model is the reprocessing model (e.g. Loeb & Ulmer 1997; Strubbe & Quataert 2009; Metzger & Stone 2016) in which an accretion disk forms when the fallback matter returns to the pericenter.<sup>7</sup> The accretion rate is larger than the Eddington rate and a massive disk wind is launched, blocking X-rays from the disk and reprocessing them to optical photons. Such a massive disk wind can be the radio outflow for the freely-coasting model. Neither optical emission model predicts outflows launched after the optical peak, as found in the decelerating model.

## 7 SUMMARY

TDE AT2019dsg presents rich data not only in the optical/UV and X-rays but also in the radio bands, thereby giving us a good opportunity to study the dynamics of the radio-emitting outflow. In this work, we revisit the radio data and results of the equipartition method carried out by Stein et al. (2021); Cendes et al. (2021). This method gives us the radius and energy within the radio-emitting site at each observation time when the SSA spectral peak is available. For the equipartition radius, we fit the evolution with linear and power-law functions representing freely-coasting and decelerating outflows, respectively. Assuming isotropic geometry, the former model gives an outflow velocity  $\simeq 1.5 \times 10^4 \text{ km s}^{-1}$ . The latter model requires  $\simeq 2.5 \times 10^4 \text{ km s}^{-1} (t/24 \text{ d})^{-0.4}$ , and the inferred CNM density distribution is shallower than that of the former one due to the different velocity evolution.

The equipartition energy increases with time. This was interpreted as due to an energy injection from the BH by Stein et al. (2021) and Cendes et al. (2021). In both the freely-coasting and decelerating models, if there is continual energy injection, it requires some sort of fine tuning. For the freely-coasting model, the CNM density profile must be matched to the rate of energy injection from the central engine in order to keep the velocity constant. For the decelerating model, the injection rate of  $\dot{E}_{\text{kin}} \propto t^{-0.4}$  is much different from the mass fallback rate to the BH. Moreover the total energy is very small compared to the overall energy budget of the system.

On the other hand, the increase in energy can be naturally interpreted as arising from the kinetic energy of the outflow. In the freely-coasting model, the outflow mass is larger than

the external mass and hence the velocity automatically remains essentially constant. As the outflow sweeps up more and more matter, the energy within the radio-emitting region increases. In this case, the external density  $n \propto R^{-2}$ . In the decelerating model, the outflow mass is small so that sweeping up material slows it down; the deceleration then results in originally-slower matter catching up, delivering additional energy.

To summarize, we find that the basic picture in which radio emission is produced by a shock running into external material naturally leads to continuing energy transfer from material driving the shock into the shocked region. Thus, in any shock-driven system in which the cooling time is longer than the dynamical time, and in particular here and in other radio TDEs, this is the simplest and most natural explanation for the gradual growth of the energy in the radio emitting region.

## ACKNOWLEDGMENTS

We thank Chi-Ho Chan, Assaf Horesh, and Christopher Irwin for fruitful discussions and helpful comments. T.M. thanks the Yukawa Institute for Theoretical Physics at Kyoto University. Discussions during the YITP workshop YITP-T-21-05 on “Extreme Outflows in Astrophysical Transients” were useful for this work. This work is supported in part by JSPS Postdoctoral Fellowship, Kakenhi No. 19J00214 (T.M.) and by ERC advanced grant “TRex” (T.P.).

## DATA AVAILABILITY

The data underlying this article will be shared on reasonable request to the corresponding author.

## REFERENCES

- Alexander K. D., Berger E., Guillochon J., Zauderer B. A., Williams P. K. G., 2016, *ApJ*, **819**, L25  
 Alexander K. D., van Velzen S., Horesh A., Zauderer B. A., 2020, *Space Sci. Rev.*, **216**, 81  
 Anderson M. M., et al., 2020, *ApJ*, **903**, 116  
 Baganoff F. K., et al., 2003, *ApJ*, **591**, 891  
 Barniol Duran R., Nakar E., Piran T., 2013, *ApJ*, **772**, 78  
 Brown J. S., Holoien T. W. S., Auchettl K., Stanek K. Z., Kochanek C. S., Shappee B. J., Prieto J. L., Grupe D., 2017, *MNRAS*, **466**, 4904  
 Cannizzaro G., et al., 2021, *MNRAS*, **504**, 792  
 Cendes Y., Alexander K. D., Berger E., Eftekhari T., Williams P. K. G., Chornock R., 2021, arXiv e-prints, p. arXiv:2103.06299  
 Cenko S. B., et al., 2016, *ApJ*, **818**, L32  
 Chevalier R. A., 1998, *ApJ*, **499**, 810  
 Gillessen S., et al., 2019, *ApJ*, **871**, 126  
 Hayasaki K., Yamazaki R., 2019, *ApJ*, **886**, 114  
 Hills J. G., 1975, *Nature*, **254**, 295  
 Holoien T. W. S., et al., 2016, *MNRAS*, **455**, 2918  
 Huang Y. F., Cheng K. S., 2003, *MNRAS*, **341**, 263  
 Jiang N., Dou L., Wang T., Yang C., Lyu J., Zhou H., 2016, *ApJ*, **828**, L14  
 Krolik J., Piran T., Svirski G., Cheng R. M., 2016, *ApJ*, **827**, 127  
 Landau L. D., Lifshitz E. M., 1987, *Fluid Mechanics*  
 Liu R.-Y., Xi S.-Q., Wang X.-Y., 2020, *Phys. Rev. D*, **102**, 083028

<sup>6</sup> They took into account the order-unity corrections due to stellar structure and relativistic effects in Eq. (10).

<sup>7</sup> However, a naive estimate of the outflow mass suggests that this model requires more mass than is typically involved in TDEs (Matsumoto & Piran 2021b).

- Loeb A., Ulmer A., 1997, *ApJ*, **489**, 573
- Matsumoto T., Piran T., 2021a, arXiv e-prints, p. [arXiv:2107.06289](#)
- Matsumoto T., Piran T., 2021b, *MNRAS*, **502**, 3385
- Metzger B. D., Stone N. C., 2016, *MNRAS*, **461**, 948
- Miller J. M., et al., 2015, *Nature*, **526**, 542
- Mohan P., An T., Zhang Y., Yang J., Yang X., Wang A., 2021, arXiv e-prints, p. [arXiv:2106.15799](#)
- Murase K., Kimura S. S., Zhang B. T., Oikonomou F., Petropoulou M., 2020, *ApJ*, **902**, 108
- Pacholczyk A. G., 1970, Radio astrophysics. Nonthermal processes in galactic and extragalactic sources
- Phinney E. S., 1989, in Morris M., ed., IAU Symposium Vol. 136, The Center of the Galaxy. p. 543
- Piran T., Svirski G., Krolik J., Cheng R. M., Shiokawa H., 2015, *ApJ*, **806**, 164
- Rees M. J., 1988, *Nature*, **333**, 523
- Roth N., Rossi E. M., Krolik J., Piran T., Mockler B., Kasen D., 2020, *Space Sci. Rev.*, **216**, 114
- Ryu T., Krolik J., Piran T., 2020a, *ApJ*, **904**, 73
- Ryu T., Krolik J., Piran T., Noble S. C., 2020b, *ApJ*, **904**, 99
- Sari R., Piran T., Narayan R., 1998, *ApJ*, **497**, L17
- Saxton R., Komossa S., Auchettl K., Jonker P. G., 2020, *Space Sci. Rev.*, **216**, 85
- Scott M. A., Readhead A. C. S., 1977, *MNRAS*, **180**, 539
- Sironi L., Giannios D., 2013, *ApJ*, **778**, 107
- Stein R., et al., 2021, *Nature Astronomy*, **5**, 510
- Stone N. C., Vasiliev E., Kesden M., Rossi E. M., Perets H. B., Amaro-Seoane P., 2020, *Space Sci. Rev.*, **216**, 35
- Strubbe L. E., Quataert E., 2009, *MNRAS*, **400**, 2070
- Winter W., Lunardini C., 2021, *Nature Astronomy*, **5**, 472
- Yalinewich A., Steinberg E., Piran T., Krolik J. H., 2019, *MNRAS*, **487**, 4083
- van Velzen S., et al., 2016, *Science*, **351**, 62
- van Velzen S., Holoiën T. W. S., Onori F., Hung T., Arcavi I., 2020, *Space Sci. Rev.*, **216**, 124
- van Velzen S., et al., 2021, *ApJ*, **908**, 4